Detailed simulations of primary breakup of turbulent liquid jets in crossflow

By M. G. Pai, O. Desjardins† AND H. Pitsch

1. Motivation and objectives

The problem of breakup of a liquid fuel in a crossflow finds relevance in applications such as lean premixed prevaporized (LPP) ducts, afterburners for gas turbines and combustors for ramjets and scramjets. Combustion efficiency and pollutant formation are directly determined by the efficient mixing of the fuel/air mixture, which is in turn controlled by the breakup of the fuel jet. Liquid jet breakup in a crossflow is a result of a complex process that includes development of instabilities along the liquid surface along with shedding of ligaments and drops from the sides of the injected liquid column. The breakup is amplified by the presence of various contributing factors: turbulence in the crossflow and liquid jet, cavitation in the injection nozzle, pressure fluctuations and aerodynamic sources.

The subject of liquid jet in crossflow (LJCF) has been the focus of several experimental studies with the primary objective of understanding the phenomenon better and proposing physical models for liquid breakup. Various regimes of liquid breakup have been observed both for turbulent and non-turbulent round liquid jets in crossflow, and the effect of variation in physical variables that characterize both the liquid jet injection and crossflow has been investigated (Sallam *et al.* 2004; Lee *et al.* 2007). From the experimental datasets, phenomenological scaling laws for various statistics such as liquid jet penetration and trajectory, Sauter mean diameter of drops and wavelength of liquid surface instabilities have been proposed. These models have also been adapted into computational fluid dynamics (CFD) calculations of gas turbine combustors and spray flames (Madabhushi *et al.* 2004; Raju 2005). Yet, predictive models for primary breakup of turbulent liquid jets that can predict a drop size distribution for a given set of inlet and ambient conditions are still unavailable. Our understanding of the precursors of ligament shedding and drop formation from the surface of the liquid jet is still inadequate to enable us to propose such models. Although experiments have shed light on some of these aspects, further investigation is necessary. It is challenging to obtain detailed measurements in the near field region (close to the injector) and inside the liquid jet that are needed to accurately quantify these precursors. It is also challenging to perform parametric experimental studies that isolate the effect of density ratio, crossflow and liquid jet Reynolds number and other non-dimensional groups related to the LJCF. Using numerical simulations, on the other hand, one can ideally explore the entire parametric space that characterizes the LJCF. With the advent of novel robust and accurate numerical methods to simulate the complex interfacial structures observed during liquid breakup and the availability of large, high-performance computational resources, one is in a position to quantify and understand fundamental mechanisms associated with liquid primary breakup with unprecedented detail.

† Department of Mechanical Engineering, University of Colorado, Boulder, Colorado, USA

In this study, we employ a recently proposed spectrally refined interface (SRI) tracking method (Desjardins & Pitsch 2008) to study liquid jets in crossflow through detailed numerical simulations. Owing to the improved resolution of the interface that is possible with this method, it has the unique capability of being able to retain fine structures that are formed during liquid primary breakup. In this work, various dimensionless groups involved in the physical problem of an LJCF are first identified. This exercise illustrates the large parameter space involved. Resolution requirements to perform detailed simulations of LJCFs are estimated. These estimates provide a glimpse of the increased computational expense incurred in performing a realistic numerical calculation of a LJCF compared to single-phase flows. From the non-dimensional parametric space, the effect of two dimensionless groups, namely the Weber numbers corresponding to the liquid jet and the crossflow, which dictate the likelihood of breakup of the liquid jet are investigated. Only bulk features of the liquid jet are studied in this work, which also helps in minimizing computational expense. This work concludes with a summary of the principal results from the study that will set the stage for further investigations on this problem.

2. Governing equations

We begin by reviewing the governing equations for the physical problem, which are the incompressible Navier-Stokes (NS) equations given by

$$\frac{\partial \mathbf{u}}{\partial t} + \mathbf{u} \cdot \nabla \mathbf{u} = -\frac{1}{\rho}\nabla p + \frac{1}{\rho}\nabla \cdot \left(\mu \left(\nabla \mathbf{u} + (\nabla \mathbf{u})^T\right)\right), \tag{2.1}$$

where $\mathbf{u}$ is the velocity, p is the pressure, ρ is the thermodynamic density and μ is the dynamic viscosity, and the continuity equation

$$\frac{\partial \rho}{\partial t} + \nabla \cdot \rho \mathbf{u} = 0 \tag{2.2}$$

and the incompressibility constraint $D\rho/Dt = 0$ imply that the velocity field is solenoidal. Other equivalent formulations of the governing equations for immiscible two-phase flows with an interface are also available (Scardovelli & Zaleski 1999). If Γ represents the interface that separates the two immiscible fluids or phases, then the following condition holds at the interface:

$$[p]_\Gamma = \sigma\kappa + \left[\mu\left(\frac{\partial u_i}{\partial x_j} + \frac{\partial u_j}{\partial x_i}\right) n_i n_j\right]_\Gamma \tag{2.3}$$

where $[Q]_\Gamma = Q_+ - Q_-$ represents the jump of a quantity Q which has values Q_+ and Q_- on either side of the interface, κ is the mean curvature, σ is the interfacial tension and $\mathbf{n}$ is the unit normal to the interface. Since we consider a liquid and a gas, we define the $(+)$ side to be in the liquid (l) and the $(-)$ side to be in the gas (g). The jump condition in Eq. (2.3) can be simplified by noting that (Kang *et al.* 2000)

$$\left[\left(\frac{\partial u_i}{\partial x_j} + \frac{\partial u_j}{\partial x_i}\right) n_i n_j\right]_\Gamma = 2\left[\frac{\partial u_i}{\partial x_j} n_i n_j\right]_\Gamma = 0 \tag{2.4}$$

resulting in

$$[p]_\Gamma = \sigma\kappa + 2\,[\mu]_\Gamma \frac{\partial u_i}{\partial x_j} n_i n_j = \sigma\kappa + 2\,[\mu]_\Gamma\, \mathbf{n}^T \cdot \nabla \mathbf{u} \cdot \mathbf{n}, \tag{2.5}$$

where $[\mu]_\Gamma$ is a constant non-zero jump in the viscosity across the interface. Since the two fluids have different densities, there is a jump in the density, i.e., $[\rho]_\Gamma$ = constant

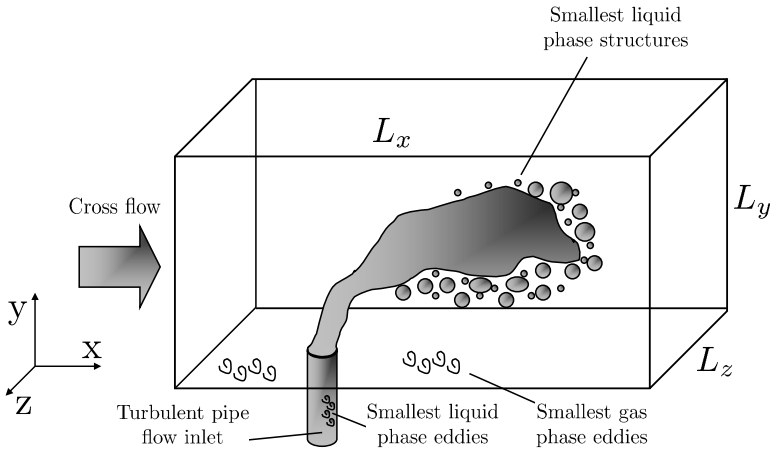

FIGURE 1. Schematic of a liquid jet in crossflow showing important length scales that need to resolved in a numerical simulation.

across the interface (we assume constant viscosity and density in the two fluids). From the conservation of mass, it follows that for a flow with no interphase mass transfer, the velocity at the interface is continuous, i.e., $[\mathbf{u}]_\Gamma = 0$.

3. Dimensionless groups

A typical LJCF consists of a jet of liquid fuel injected transversely into a gaseous crossflow as shown in Fig. 1. Although the problem may seem simple at first, there are 8 dimensional variables of interest in this problem. These are the thermodynamic densities of the liquid and gaseous phases denoted ρ_l and ρ_g, respectively, absolute viscosities of the liquid and gaseous phases denoted μ_l and μ_g, respectively, diameter of the injector denoted d, velocities of the liquid and gaseous phases denoted $\mathbf{U}_l$ and $\mathbf{U}_g$ at inlet planes, respectively, and the interfacial surface tension denoted σ. The following dimensionless groups are relevant to LJCFs:

$$\text{Crossflow Weber number:} \qquad We_{\text{cf}} = \frac{\rho_g \, \langle U_{g,x} \rangle^2 \, d}{\sigma} = \frac{\text{inertia (gas)}}{\text{surface tension}} \tag{3.1}$$

$$\text{Liquid Weber number:} \qquad We_{\text{liq}} = \frac{\rho_l \, \langle U_{l,y} \rangle^2 \, d}{\sigma} = \frac{\text{inertia (liq)}}{\text{surface tension}} \tag{3.2}$$

$$\text{Crossflow Reynolds number:} \qquad Re_{\text{cf}} = \frac{\rho_g \langle U_{g,x} \rangle d}{\mu_g} = \frac{\text{inertia (gas)}}{\text{viscous (gas)}} \tag{3.3}$$

$$\text{Liquid Reynolds number:} \qquad Re_{\text{liq}} = \frac{\rho_l \langle U_{l,y} \rangle d}{\mu_l} = \frac{\text{inertia (liq)}}{\text{viscous (liq)}} \tag{3.4}$$

$$\text{Momentum flux ratio:} \qquad q = \frac{\rho_l}{\rho_g} \left(\frac{\langle U_{l,y} \rangle}{\langle U_{g,x} \rangle} \right)^2 = \frac{We_{\text{liq}}}{We_{\text{cf}}} \tag{3.5}$$

$$\text{Density ratio:} \qquad \phi = \frac{\rho_l}{\rho_g} \tag{3.6}$$

$$\text{Ohnesorge number:} \qquad Oh = \frac{\mu_l}{\sqrt{\rho_l d\sigma}} = \frac{\text{viscous (liq)}}{\text{surface tension}} \tag{3.7}$$

$$\tag{3.8}$$

Here, $\langle U_{l,y} \rangle$ is the y component of the liquid mean velocity $\langle \mathbf{U}_l \rangle$ at injection and $\langle U_{g,x} \rangle$ is the x component of the gas phase mean velocity $\langle \mathbf{U}_g \rangle$ at injection. For brevity of notation, the angled brackets are omitted from the rest of the discussion with the implicit understanding that $U_l = \langle U_{l,y} \rangle$ and $U_g = \langle U_{g,x} \rangle$. One may observe from Eq. (3.5) that of the three dimensionless groups q, We_{cf} and We_{liq}, only two are independent. Furthermore, from among the three dimensionless groups Oh, Re_{liq} and We_{liq}, only two are independent since

$$We_{\text{liq}} = Oh^2 Re_{\text{liq}}^2. \tag{3.9}$$

So, effectively there are five dimensionless groups of interest in this problem. Therefore in order to completely characterize a LJCF, a comprehensive study will have to span the entire five-dimensional parametric space.

4. Computational expense

Numerical resolution requirements for an LJCF are primarily dictated by the choice of inlet flow parameters for the gas and liquid phase, and the need to resolve the smallest liquid and gas phase structures in the bulk of the domain. For this exercise, we assume a uniform grid throughout the computational domain, thereby providing us with an upper (or conservative) estimate for the grid resolution required in the computational domain.

4.1. *Resolution of liquid-phase eddies at injection*

A turbulent pipe inflow is employed as an inlet condition for the liquid fuel, so the need to resolve the smallest liquid phase length scales decides the resolution close to the injector. The smallest scales in the turbulent pipe flow are characterized by the friction Reynolds number $Re_\tau = d/\delta_v$, where δ_v is the viscous length scale. We intend to develop a scaling for the number of grid points across the injector diameter $N_{\text{dia}} = d/\Delta x$ with Re_{liq}, where Δx is the uniform grid spacing in the computational domain and along the diameter of the pipe. We use the following relationship between the friction factor f and Re_τ

$$f = 8 \left(\frac{Re_\tau}{Re_{\text{liq}}} \right)^2 \tag{4.1}$$

and the Blasius fit

$$f = 0.3164 \, Re_{\text{liq}}^{-1/4}, \tag{4.2}$$

which is a good approximation for $2000 < Re_{\text{liq}} < 10^5$ (Mckeon *et al.* 2004). Assuming an equality between Eq. (4.1) and Eq. (4.2) over this range of Re_{liq}, the relationship between Re_τ and Re_{liq} can be approximated as

$$Re_\tau = 0.19887 \, Re_{\text{liq}}^{7/8}. \tag{4.3}$$

Assuming $\Delta x = 2\delta_v$, we obtain a scaling for N_{dia} with Re_{liq} as

$$N_{\text{dia}} = 0.1 \, Re_{\text{liq}}^{7/8}. \tag{4.4}$$

The scaling suggests that for $Re_{\rm liq} = 5000$ a uniform mesh resolution of $N_{\rm dia} = 172$ is required across the injector diameter, while for $Re_{\rm liq} = 1 \times 10^4$ the requirement increases to $N_{\rm dia} = 315$. We expect that this conservative estimate for the resolution can be reduced since the liquid length scales in the pipe flow begin to increase soon after the jet ejects from the confines of the pipe into the crossflow, analogous to a single-phase round jet (also see numerical simulations of single-phase plane jets of Da Silva & Mètais (2002) where they employ a grid size of 30 grid points for a jet Reynolds number of 3000.) So, we expect that the maximum attainable $Re_{\rm liq}$ for a given $N_{\rm dia}$ can be increased by a factor of r, where r is tentatively fixed to be 3 for the preliminary runs, and yet be able to resolve all the important length scales arising from the Reynolds number requirement. This hypothesis will be carefully studied in subsequent investigations.

4.2. *Resolution of liquid-phase structures*

For droplet-laden flows, the liquid Weber number decides the competitive effects of inertia and surface tension forces and thus the likelihood of a drop to undergo further breakup. Theoretical analyses (Hinze 2000) and experiments (Lefebvre 1998) suggest that drops with liquid Weber number less than ~ 10 do not undergo further breakup. The need to resolve droplets (or liquid structures) until this limit imposes a requirement on the smallest grid size in the computational domain. In other words, we require that the Weber number based on the grid size Δx, $We_{\Delta x}$, be less than 10, i.e., $We_{\Delta x} = \rho_l U_l^2 \Delta x/\sigma < 10$ from which a criterion on $N_{\rm dia}$ arises as

$$N_{\rm dia} > 0.1 We_{\rm liq}. \tag{4.5}$$

Normally, the crossflow Weber number ($We_{\rm cf}$) is less than the liquid Weber number ($We_{\rm liq}$), so the above requirement for $N_{\rm dia}$ based on $We_{\rm liq}$ is more restrictive.

Since the SRI method provides subcell resolution (see Sect. 5) liquid structures smaller than a (velocity-pressure) cell can be retained. This implies that one may access p times larger Weber numbers, where $p + 1$ is the number of quadrature nodes in each cell, by adopting the subcell resolution. Obviously, the velocity and pressure around these subcell structures are not captured accurately. It is expected that this relaxed resolution will not affect the overall behavior of the liquid jet since in this study we focus on large scale features of the liquid jet.

4.3. *Resolution of gas-phase eddies*

In experiments on LJCF, typical gas-phase Reynolds numbers based on the hydraulic diameter of the test section are $\mathcal{O}(1e5)$. Owing to the expected significant computational expense incurrred in detailed simulations, we do not plan to model the entire test section which can be as large as 10-100 times the injector diameter. Using the mean gas-phase velocities quoted in the experiments, we deduce a gas-phase Reynolds number based on the injector diameter $Re_{\rm cf}$ (as defined earlier in Sec. 3) for comparison with our computation. In the preliminary investigations, we choose experimental datasets such that $Re_{\rm cf} \leq Re_{\rm liq}$, and so we expect the smallest gas-phase eddies to be resolved in the domain if Eq. (4.4) is satisfied.

4.4. *Total grid size for the computational domain*

For a uniform grid, the total number of grid points in the entire computational domain is given as (see Fig. 1) $N_{\rm tot} = L_x L_y L_z/(\Delta x)^3$. Based on the foregoing results, the above

relation can be rewritten as

$$N_{\text{tot}} = n_x n_y n_z \max\left(0.001We_{\text{liq}}^3/p^3,\ 0.001Re_{\text{liq}}^{21/8}/r^3\right), \tag{4.6}$$

where n_x, n_y and n_z are the lengths of the domain in the x, y and z directions, respectively, in multiples of diameter d. An estimate for the penetration of the liquid jet along the liquid streamwise (y) direction that would decide L_y is (Sallam *et al.* 2004)

$$\frac{y}{d} = n_y = C_{yb}\, q^{1/2}, \tag{4.7}$$

where $C_{yb} = 2.5$. The same study also proposes an estimate for the penetration of the liquid jet along the crossflow (x) direction as $x/d = n_x = C_{xb}$, where $C_{xb} = 7.5$.

Thus, an estimate for the grid size required in the entire computational domain is

$$N_{\text{tot}} = (C_{xb} + n_{xb})(C_{yb} + n_{yb}) n_z q^{1/2} \max\left(0.001We_{\text{liq}}^3/p^3,\ 0.001Re_{\text{liq}}^{21/8}/r^3\right), \tag{4.8}$$

where $n_{xb} = 3$ and $n_{yb} = 4$ represent an additional buffer region upstream of the injector inlet for the flow to develop around the liquid column, and along the y direction, respectively. Sensitivity of the results to the size of the buffer region will be tested in subsequent studies.

The above estimate for the total grid size highlights the high computational cost compared to single-phase non-reacting flow that is incurred in performing detailed simulations of a LJCF, if one intends to resolve important physical length scales of the problem. Note that the Weber number scales like U^2 whereas the Reynolds number scales like U, which suggests that the Weber number may more likely impose a stricter requirement on the resolution. This clearly indicates the need for large parallel computing resources for such problems, in addition to accurate and robust computer codes that exhibit good scaling characteristics with problem size on these computers.

5. Numerical method

Interface tracking techiques (Sethian 1999; Osher & Fedkiw 2003) have been found to be very attractive for simulating immiscible two phase flows. In this study, a spectrally refined interface tracking scheme is employed (Desjardins 2008). This interface tracking technique has several advantages over other methods currently available in literature such as the volume of fluid (VOF) (Scardovelli & Zaleski 1999), coupled level set/volume of fluid (CLSVOF) (Sussman *et al.* 2007) and Lagrangian particle-based methods (Hieber & Koumoutsakos 2005) (see Desjardins (2008) for a detailed discussion). In SRI, the level set field is represented on a finite number of subcell quadrature nodes around the interface. The level set field is advected using a semi-Lagrangian approach which consists in observing that the level set equation given by

$$\frac{\partial G}{\partial t} + \mathbf{u}\cdot\nabla G = \frac{DG}{Dt} = 0, \tag{5.1}$$

where $G(\mathbf{x}, t)$ is the level set field, should be a constant along the trajectory of material points moving at velocity $\mathbf{u}$. At the new location $\mathbf{x}^{n+1}$ and time t^{n+1}, the value of the level set function corresponding to each quadrature node is computed by integrating backward in time to the previous position $\mathbf{x}^n$ at t^n along the material point trajectory that passes through $\mathbf{x}^{n+1}$. The value of $G^{n+1}(\mathbf{x}^{n+1})$ is then set equal to G^n at location $\mathbf{x}^n$. Since high-order schemes can be used to numerically integrate along the material point trajectory, numerical diffusion of the interface is minimal. This method, in conjunction

Cases	q	$We_{\rm cf}$	$We_{\rm liq}$	$N_{\rm tot}$ (million cells) ($N_x \times N_y \times N_z$)	$L_x \times L_y \times L_z$ (times d)	$N_{\rm proc}$	Regime
(A)	5	100	500	36 ($420 \times 340 \times 256$)	$12 \times 10 \times 7$	256	M/S
(B)	10	100	1000	45 ($420 \times 420 \times 256$)	$12 \times 12 \times 7$	256	M/S
(C)	10	300	3000	45 ($420 \times 420 \times 256$)	$12 \times 12 \times 7$	256	S/C
(D)	30	100	3000	64 ($420 \times 600 \times 256$)	$12 \times 16 \times 7$	768	S/C
(E)	100	30	3000	110 ($420 \times 1024 \times 256$)	$12 \times 28 \times 7$	1024	S/C

TABLE 1. Parameters of the test cases for varying momentum flux ratios, crossflow Weber number and liquid Weber numbers. Injection Reynolds number $Re_{\rm liq} = 5000$ for all the cases. M/S denotes "multimode/ shear breakup transition"; S/C denotes "surface/ column breakup transition". $N_{\rm proc}$: total number of processesors used for each computation. Case (C) has also been performed with twice the mesh resolution of approximately 240 million cells on 2048 processes.

with the subcell resolution, enables retaining sharp features of the interface as the liquid jet evolves in time (see Desjardins & Pitsch (2008) for details).

A high-order conservative finite difference scheme (Desjardins *et al.* 2007) is built into an in-house code called NGA, which has been efficiently written with MPI libraries for large-scale distributed memory computations. The variables are staggered in space and time, and centered finite difference schemes are employed. Accurate jump conditions for the pressure given by Eq. (2.5) that include the surface tension force are imposed using a ghost fluid (GF) method (Desjardins *et al.* 2008). Only second-order accuracy will be employed here since the formal order of accuracy is limited by the interfacial GF treatment, which is currently first-order. In order to allow for an implicit treatment of the viscous terms in the NS equations in conjuction with an approximate factorization technique, we adopt a continuous surface force (CSF) formulation for the viscosity. This essentially removes the jump in viscosity in Eq. (2.5) and thus the pressure jump contains only the surface tension.

6. Results

In this preliminary study, we isolate the effects of the crossflow and liquid Weber numbers on the evolution of the liquid jet from the complete parametric space. The crossflow Weber number characterizes, in comparison to surface tension forces, the tendency of the crossflow inertia forces to break the liquid jet, while the liquid Weber number characterizes the tendency of the liquid jet inertia to break the jet. A series of five simulations for varying momentum flux ratios, liquid Weber numbers and crossflow Weber numbers, details of which are provided in Table 1, is performed. In the table, cases (A), (B) and (D) correspond to constant $We_{\rm cf}$ cases for varying q and $We_{\rm liq}$, while cases (C), (D) and (E) correspond to constant $We_{\rm liq}$ for varying q and $We_{\rm cf}$.

6.1. *Computational domain and run details*

To avoid loss of liquid mass due to grid stretching, a uniform grid is employed around the injector for the expected penetration length of the liquid jet given by Eq. (4.7) for each case. From there onward until the end of the domain, a gradual 1% stretch in the mesh

is introduced. The computational domain consists of the crossflow inlet plane (y-z plane) as shown in Fig. 1 where a laminar boundary layer profile is prescribed. Liquid injection along the y direction (x-z plane) is a turbulent pipe inflow at a mean Reynolds number of 5000. The turbulent pipe inflow is delivered into the crossflow through an nozzle of length $2d$ so that the interaction of the crossflow with the turbulent pipe flow close to the injector exit is captured. Open boundary conditions are applied in the cross-stream directions along the z direction, and at the top x-z plane (along the y direction).

For the maximum liquid Weber number of 3000 in our study, an estimate for the resolution across the injector diameter based on Eq. (4.5) and $p = 4$ is 75. However, for this preliminary study and to minimize computational expense, we use $N_{\text{dia}} = 40$, which is about half the estimated resolution. This essentially implies that one can expect the smallest drops produced in the simulations to break up further. However, since the focus of this preliminary study is not on quantifying the drop size distribution, we accept this resolution as reasonable to predict penetration length and large scale features of the jet. Also, the estimate for the resolution based on the liquid phase Reynolds number is $N_{\text{dia}} = 57$, which is again slightly larger than that used in the simulations. The effect of the varying grid resolution will be explored in a subsequent study.

We choose the parameters of the simulation so that they are close to the experimental datasets provided to us by collaborators at UTRC. A density ratio of $\rho_l/\rho_g = 10$ is used for all simulations presented in this study (cf. experimental value of 642). For this study, we choose the viscosity of the gas such that the kinematic viscosity ratio $(\mu_l/\mu_g)(\rho_g/\rho_l)$ is close to the experimental value of 0.07. The injector diameter is chosen to be 0.48 mm, which matches with the experiment. The ratio of viscous to surface tension forces given by the Ohnesorge number is < 0.01 for all cases, so that surface tension forces dominate the problem physics.

For the NS equations, an approximate factorization method is used to implicitly solve the predictor step of the fractional step method. For the pressure solution, the PCG+PFMG combination from the Hypre suite of parallel preconditioners (Falgout & Yang 2002) with a pressure convergence criterion of 1×10^{-10} is employed. Average wall-clock time per computational time step varies from 20 seconds for the smallest domain (36 million cells over 256 processes) to around 40 seconds for the largest domain (240 million cells over 2048 processes) studied.

6.2. *Discussion of results*

6.2.1. *Visualization*

Figure 2 shows the evolution of the liquid jet for four cases. For cases (A), (B) and (D) (see Figs. 2(a), 2(b), 2(d)), the liquid Weber numbers We_{liq} are 500, 1000 and 3000, respectively. Comparing the three cases, one can clearly observe that with increasing We_{liq}, the size of liquid structures that break off the liquid column decreases. Since We_{cf} is constant across the three cases, the tendency of the crossflow inertia to breakup the liquid jet is the same. Therefore, the smaller liquid structures are clearly due to the increasing We_{liq}. With increasing momentum flux ratio q, the jet penetrates deeper into domain, which agrees with experiments (see quantitative comparison later). Figures 3(a), 3(b) and 3(c) show the windward side of the liquid jets for the three cases, clearly revealing the decreasing size of liquid surface disturbances with increasing We_{liq}. We compare predictions of the characteristic length scale of these disturbances with experiments later.

Figures 2(c), 2(d) and 4(a) corresponding to cases (C), (D) and (E) show the evolution of the liquid jet for constant liquid Weber number and crossflow Webers number of 300,

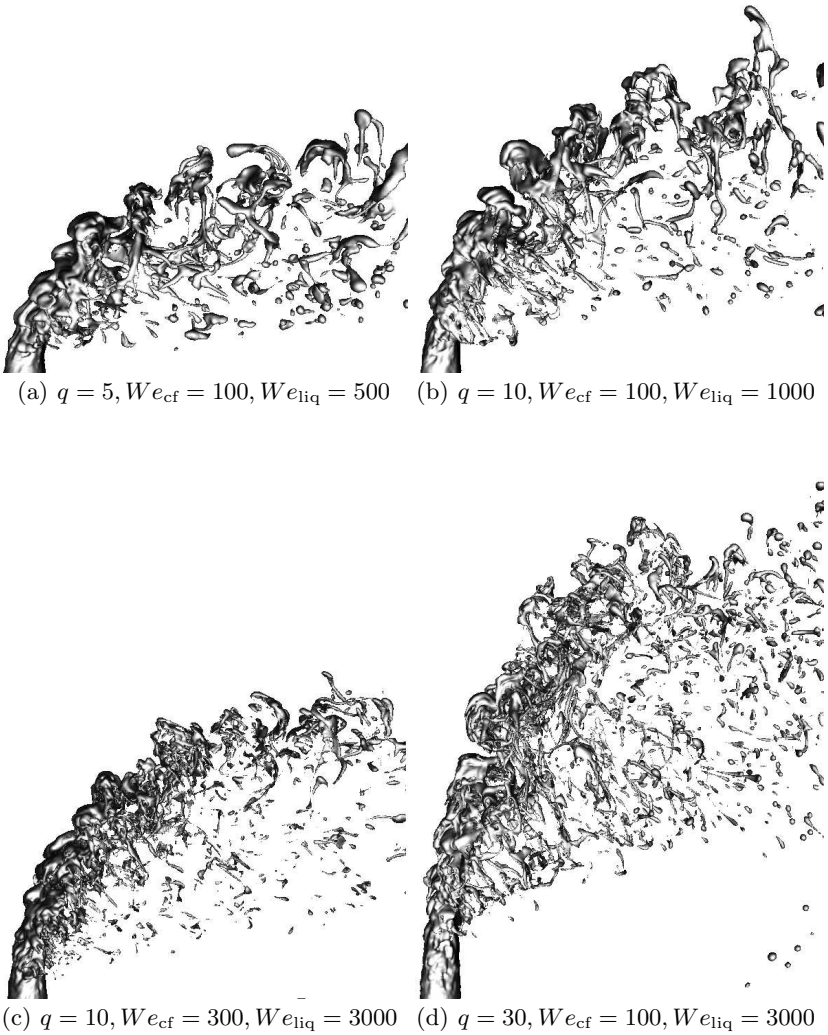

(a) $q = 5, We_{\mathrm{cf}} = 100, We_{\mathrm{liq}} = 500$ (b) $q = 10, We_{\mathrm{cf}} = 100, We_{\mathrm{liq}} = 1000$

(c) $q = 10, We_{\mathrm{cf}} = 300, We_{\mathrm{liq}} = 3000$ (d) $q = 30, We_{\mathrm{cf}} = 100, We_{\mathrm{liq}} = 3000$

FIGURE 2. Evolution of the liquid jet in crossflow for varying q, We_{cf} and We_{liq} (Cases (A), (B), (C), (D)).

100 and 30, respectively. Similar-sized droplets and ligaments appear to be shed from the liquid column for the three cases. The size of liquid surface disturbances along the liquid jet surface (see Figs. 3(c), 3(d) and 3(e)) also show a certain visual similarity.

A typical behavior of all the jets simulated in this study is illustrated by means of a longitudinal slice through the liquid jet in Fig. 4(b). The ejected round liquid jet gradually flattens out transverse to the direction of the crossflow. Once flattened, ligament and drops are shed from the sides (see gray arrow in figure depicting the start of ligament

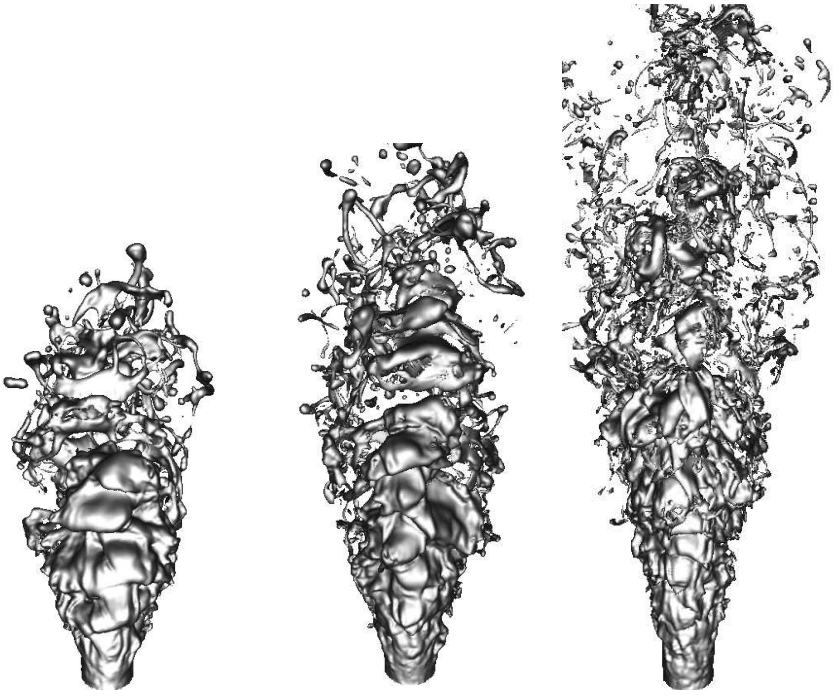

(a) $q = 5, We_{\mathrm{cf}} = 100$ (b) $q = 10, We_{\mathrm{cf}} = 100$ (c) $q = 30, We_{\mathrm{cf}} = 100$

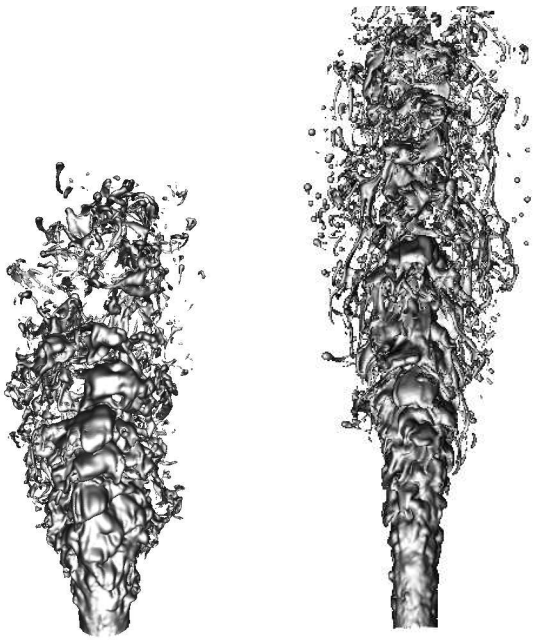

(d) $q = 10, We_{\mathrm{cf}} = 300$ (e) $q = 100, We_{\mathrm{cf}} = 30$

FIGURE 3. Windward side of liquid jet showing disturbances on the liquid surface.

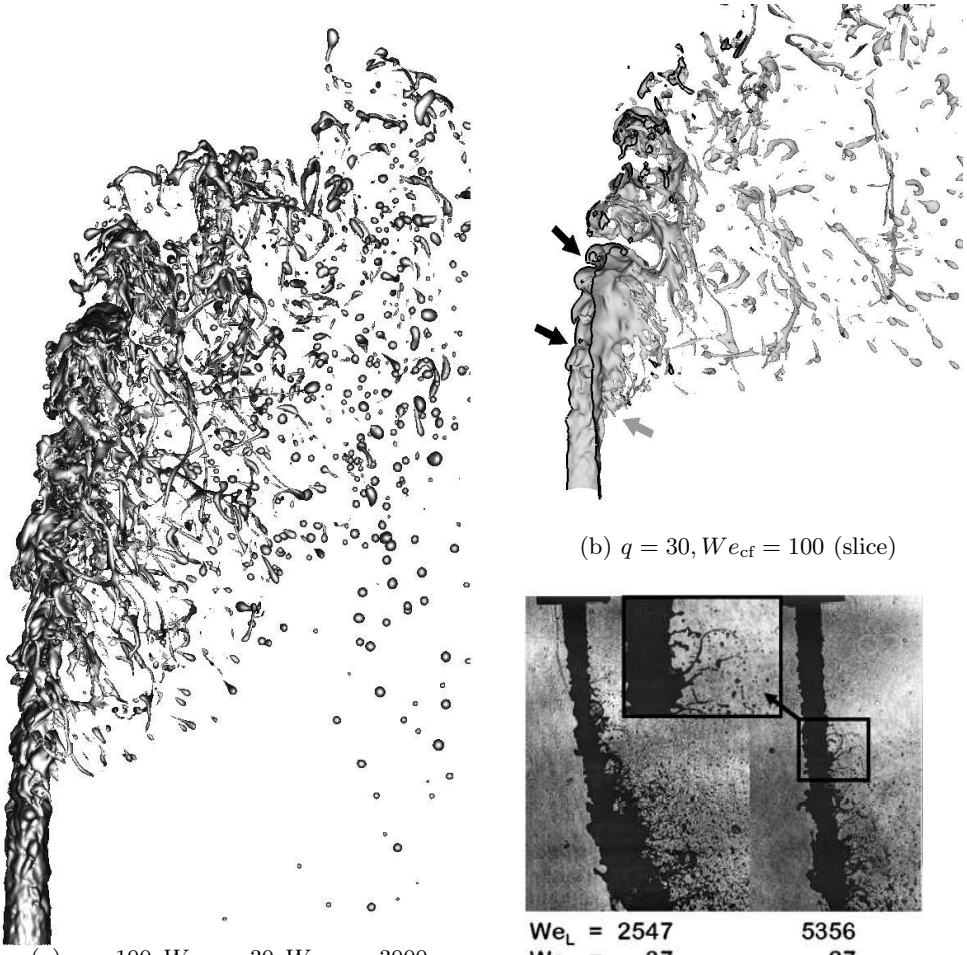

(a) $q = 100, We_{\rm cf} = 30, We_{\rm liq} = 3000$

(b) $q = 30, We_{\rm cf} = 100$ (slice)

(c)

FIGURE 4. Evolution of the liquid jet in crossflow for varying q, $We_{\rm cf}$ and $We_{\rm liq}$ - Case (E) is shown in Fig. 4(a). Figure 4(b) shows a slice through the liquid jet for Case (D) (sliced edges have been darkened to improve clarity). Black arrows point to a KH-like instability on the windward side of the jet, while the grey arrow shows the location where ligaments and drops start to break off the column. Fig. 4(c) is a snapshot from an experiment on round turbulent liquid jets in cross flow from Lee *et al.* (2007) showing thin ligaments breaking off the liquid column (read $We_L = We_{\rm liq}$ and $We_G = We_{\rm cf}$).

shedding). Figure 4(c) shows a snapshot from a typical experiment of Lee *et al.* (2007) that confirms the formation of thin ligaments from the sides of the liquid column. On the windward side of the liquid jet, frequent events of complex roll-up of the liquid interface (see black arrows) that resemble a Kelvin-Helmholtz (KH) instability are observed. These instabilities grow along the liquid jet surface ultimately breaking off the liquid column into large ligaments and droplets. The leeward side of the jet, on the other hand, exhibits only rare events of interface roll-up, especially near the beginning of liquid column breakup.

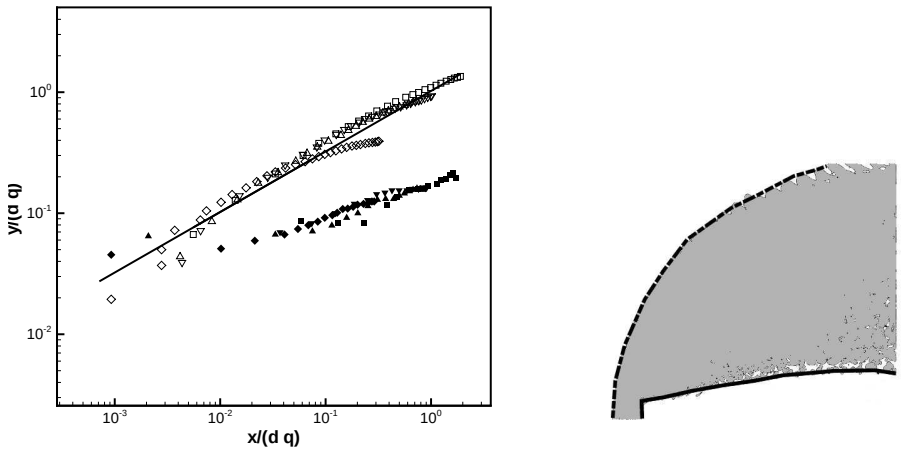

(a) (b)

FIGURE 5. Trace of liquid trajectories across all the test cases shown alongside the scaling from Lee *et al.* (2007) (solid line). Also shown is the trajectory of the lowermost extent of the spray (filled symbols). Figure 5(b) illustrates how the trajectory (dashed line) and the lowermost extent (solid line) was inferred from a superposition of several spray images. Symbols represent: □- Case (A) (q=5, $We_{\rm cf}$=100); △- Case (B) (q=10, $We_{\rm cf}$=100); ∇- Case (C) (q=10, $We_{\rm cf}$=300); ◇- Case (D) (q=30, $We_{\rm cf}$=100).

6.2.2. *Liquid jet trajectory*

A comparison of the predicted liquid trajectories for all the cases studied is shown in Fig. 5. Several snapshots of the liquid jet are first superposed over each other. The maximum extent of the liquid jet along the y-direction in the superposed image is used to infer the liquid trajectory (see Bellofiore (2006) for instance). Shown as a solid line is a scaling for the liquid jet trajectories proposed by Lee *et al.* (2007). The trajectory for Case (E) is not plotted, as the number of images accumulated were not sufficient to infer an unambiguous trajectory. Good agreement with the scaling is observed, although for Case (D), a discrepancy is observed at large $x/(dq)$. This suggests that the estimate for the computational domain length from Eq. (4.7) and the buffer of nearly $2d$ along the y-direction above the liquid jet is insufficient for this case and will be investigated in a future study. Also shown in the same figure is the trajectory of the lowermost extent of the spray inferred from the superposed image (see caption of Fig. 5(b) for details). The simulations predict the lower extent of the liquid jet on these scaled coordinates to be nearly the same across the test cases considered.

6.2.3. *Liquid surface disturbances*

From the simulations, the characteristic length scale of the KH-like instability presented in Fig. 4(b) can be measured along the liquid jet trajectory. We choose the measurement location as the point where ligaments first begin to shed from the liquid column. Sallam *et al.* (2004) measure the length scale of these disturbances experimentally for round non-turbulent liquid jets and propose a scaling of the form $\lambda/d = C_1 We_{\rm cf}^{-0.45}$ for $We_{\rm cf} > 4$, where λ is the wavelength of the disturbance and C_1 is a constant (although not clear from their article, we presume that they measure the wavelength λ at the location where the first ligaments begin to shed from the liquid column). For constant $We_{\rm liq}$, we find from Fig. 6(a) that the predicted wavelength is almost constant across the range

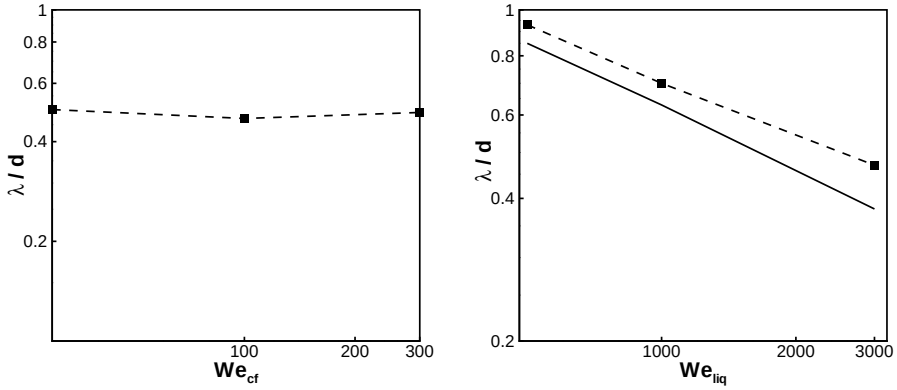

(a) Constant We_{liq} (b) Constant We_{cf}

FIGURE 6. Predicted wavelength of liquid surface disturbances on the windward side of liquid jet shown as a dashed line with symbols for (a) constant We_{liq} and (b) constant We_{cf}. Solid line: scaling $\lambda/d = C_2 We_{\mathrm{liq}}^{-0.45}$.

of We_{cf} explored in this study, which does not appear to agree with the experimental scaling. Interestingly, as shown in Fig. 6(b) for constant We_{cf}, the predicted wavelength scales like $\lambda/d = C_2 We_{\mathrm{liq}}^{-0.45}$, where C_2 is a constant different from C_1. Note that the exponent matches with that proposed by Sallam *et al.* (2004). This apparent inconsistency between the numerical results and experiments can be resolved by noting that in Fig. 3 of Sallam *et al.* (2004), the We_{liq} is not held constant across the range of We_{cf} investigated in their experiment. In fact, if the liquid Weber number corresponding to each symbol in the figure is computed, one may observe that the We_{liq} is actually increasing in the direction of increasing We_{cf}. In other words, Fig. 3 in Sallam *et al.* (2004) actually shows a decreasing λ for increasing We_{liq} and this behavior agrees with our numerical simulations. This result alone shows that if the effect of each non–dimensional group on the liquid jet evolution is not carefully isolated, then phenomenological scaling laws such the one proposed in Sallam *et al.* (2004) for the wavelength of the liquid surface disturbances can be misinterpreted.

6.2.4. *Liquid mass evolution*

A prime concern with any interface tracking scheme that is used to simulate two-phase flows is its ability to numerically conserve liquid mass (or volume). Reinitialization schemes such as the one employed in Desjardins *et al.* (2008) ensure that minimum liquid mass is lost, but at the expense of accurate breakup physics. The SRI method on the other hand ensures that small ligaments and droplets are retained in the domain, but this places a stringent requirement on the underlying grid to numerically conserve mass. Insight into the behavior of the liquid jet for varying We_{cf} and We_{liq} can be gained by computing the evolution of liquid mass in the domain. Figure 7 shows the evolution of computed liquid mass scaled by the expected liquid mass for the various test cases. The expected liquid mass $m_a(t)$ is computed by using the mean flow rate of the liquid through the injector, while the actual liquid mass $m(t)$ is computed using only the part of the liquid phase that is resolved on the velocity-pressure grid cells. This clearly neglects all the small scale features that entirely lie on the subcell quadrature points, thereby underestimating the actual mass in the domain. However, we can make some interesting

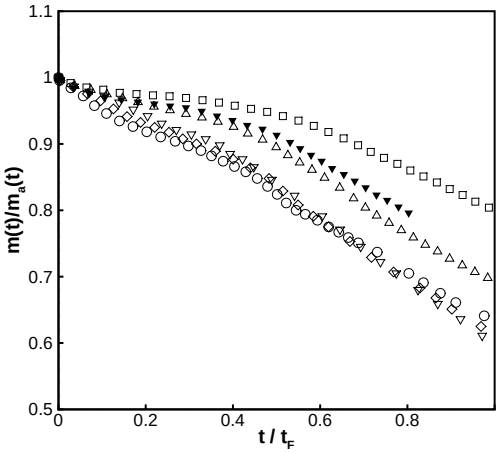

FIGURE 7. Evolution of scaled liquid mass at the velocity-pressure grid nodes. $m(t)$: actual mass of liquid in the domain (see discussion in Sec. 6.2.4), $m_a(t)$: expected mass of liquid in the domain, $t_{\rm F}$: time taken by the liquid jet to reach the end of the domain along the x direction. For symbol definitions, see Fig. 5. Additionally, ◯- Case (E) (q=100, $We_{\rm cf}$=30); ▼- Case (C) (refined grid).

observations even with this approximation. An accurate estimate (at least second–order accurate) for the mass that lies in the subcell quadrature points will require one to infer the liquid volume from the reconstructed interface front and will be pursued as a part of the future study. The time coordinate t is scaled by the time taken by each liquid jet to reach the end of the domain t_F along the streamwise direction.

From the figure, we observe that with increasing liquid Weber number, the amount of mass in the computational domain decreases, with the highest mass being observed for Case (A) (q=5, $We_{\rm cf}$=100). Clearly, if the grid resolution is increased the scaled mass evolution is closer to unity, which is illustrated for Case (C) in the same figure. For this case, with twice the grid resolution (nearly 240 million cells with $N_{\rm dia} = 80$) the amount of liquid mass in the domain increases from $\sim$ 70% to $\sim$ 80% at $t/t_F = 0.8$. Although this increased resolution appears sufficient from the scaling argument in Eq. (4.5), the mass evolution is still not around unity since the simulations suggest that, for the test Case (C), very thin elongated structures (and not small spherical droplets) are created during liquid breakup, and these thin structures quickly fall into the subcell resolution. The liquid mass conservation characteristics in this study agree with those observed in the diesel jet simulations of Desjardins (2008).

From Fig. 7 we did note that for increasing liquid Weber number, lesser liquid mass is retained in the domain; however if the liquid Weber number is kept constant, the mass evolution is the same (compare cases (C), (D) and (E), hollow symbols) for the conditions used in this study. Interestingly, the crossflow Weber number is different for cases (C), (D) and (E). The simulations predict that the amount of liquid mass at the subgrid quadrature points is on average the same for the three cases. This observation may point to an interesting conclusion that under certain conditions, the size of the smallest liquid structures may be controlled solely by the liquid Weber number and less by the crossflow Weber number, although more resolved simulations are needed to show this conclusively.

7. Conclusions and future work

Preliminary numerical simulations of liquid jet in crossflow were performed using the spectrally refined level set method. This study was done primarily to understand the feasibility of the new interface tracking methodology to handle the complex interface evolution observed in an LJCF. A parametric study to isolate the effect of crossflow and liquid Weber numbers was performed. Liquid features such as thin ligaments observed in snapshots from the computed liquid jet evolution agree with observations from experiments. Predicted liquid trajectories match well with experimental datasets, although the results need to be reconfirmed at higher grid resolution and larger domain sizes. For a constant crossflow Weber number, predicted sizes of liquid surface disturbances on the windward side of the liquid jet decrease with increasing liquid Weber number. On the other hand, for a constant liquid Weber number, variation of crossflow Weber number does not affect the predicted characteristic length scale of the disturbance. Based on the numerical predictions, it appears that the liquid Weber number controls the size of the disturbances on the windward side of the liquid jet, rather than the crossflow Weber number. An apparent inconsistency of the numerical results with a phenomenological scaling law for the wavelength of the liquid surface disturbance is resolved. This exercise suggests that scaling laws obtained from either experiments or numerical simulations that do not carefully isolate the effects of non-dimensional groups on liquid jet evolution can be misinterpreted. The numerical simulations further suggest that for the conditions chosen in the study, the liquid Weber number, on average, controls the smallest liquid length scales in the problem. More insight into the role of the crossflow and liquid Weber numbers can be obtained by quantifying the variation of liquid volume distribution and subcell distribution of liquid volume in the domain with Weber number, which will be pursued in a future study.

This study illustrates the utility of numerical simulations in understanding fundamental phenomena associated with liquid breakup in cross flows. Furthermore, as demonstrated in this work, studies that isolate the effect of a non-dimensional group can be easily performed using such numerical simulations. Future studies will focus on isolating the effect of liquid jet Reynolds number, crossflow Reynolds number and density ratio on the behavior of the liquid jet. The ultimate goal of this exercise is to propose predictive models for LJCFs based on the insight gained from such numerical simulations about the fundamental mechanisms of liquid breakup.

Acknowledgements

We thank Dr. Marco Arienti and Dr. Ravi Madabhushi of UTRC for the several discussions on the experimental datasets and insightful suggestions on comparing the datasets with numerical simulations. Funding from UTRC and NASA is also acknowledged. M. G. Pai acknowledges the help and useful discussions with Mr. S. Shashank at various stages during the development of the code capabilities for simulating the LJCF. Computational resources for numerical simulations were made available on TACC-Ranger at The University of Texas, Austin, through a NSF computer time grant.

REFERENCES

Bellofiore, A. 2006 Experimental and numerical study of liquid jets injected in high-density air crossflow. Ph.D. thesis, University of Naples.

Da Silva, B. & Métais, O. 2002 On the influence of coherent structures upon interscale interactions in turbulent plane jets. *J. Fluid Mechanics* **473**, 103–145.

Desjardins, O., Blanquart, G., Balarac, G. & Pitsch, H. 2007 High order conservative finite difference scheme for variable density low Mach number turbulent flows. *J. Comp. Phys.* **227** (15), 7125–7159.

Desjardins, O. 2008 Numerical methods for liquid atomization and application in detailed simulations of a diesel jet. Ph.D. thesis, Stanford University.

Desjardins, O., Moureau, V. & Pitsch, H. 2008 An accurate conservative level set/ghost fluid method for simulating turbulent combustion. *J. Comp. Phys.* **227** (18), 8395–8416.

Desjardins, O. & Pitsch, H. 2008 A spectrally refined interface approach for simulating multiphase flows. *J. Comp. Phys.* (accepted).

Falgout, R. D. & Yang, U. M. 2002 "HYPRE: a library of high performance preconditioners." In Computational Science - ICCS 2002 Part III, P. M. A. Sloot, C. J. K. Tan, J. J. Dongara & A. G. Hoekstra, editors. **2331** Berlin: Springer-Verlag, 632–641.

Hieber, S. E. & Koumoutsakos, P. 2005 A Lagrangian particle level set method. *J. Comp. Phys.* **210**, 342–367.

Hinze, J. O. 1955 Fundamentals of the hydrodynamic mechanism of splitting in dispersion processes. *A. I. Ch. E. Journal* **1** (3), 289–295.

Kang, M., Fedkiw, R. P. & Liu, X-D 2000 A boundary condition capturing method for Multiphase Incompressible Flow. *J. Scientific Computing* **15** (3), 323–360.

Lefebvre, A. 1998 *Gas turbine combustion.* New York: Taylor & Francis.

Lee, K., Aalburg, C., Diez, F. J., Faeth, G. M. & Sallam, K. A. 2007 Primary breakup of turbulent round liquid jets in uniform crossflows. *AIAA Journal.* **45** (8), 1907–1916.

Madabhushi, R. K., Leong, M. Y. & Hautman, D. J. 2004 Simulation of the breakup of a liquid jet in crossflow at atmospheric conditions. *Proceedings of ASME Turbo Expo 2004.* American Society of Mechanical Engineers. Vienna, Austria.

McKeon, B. J., Swanson, C. J. & Zagarola, M. V. 2004 Friction factors for smooth pipe flow. *J. Fluid Mechanics* **511**, 41–44.

Osher, S. & Fedkiw, R. 2003 Level set methods and dynamic implicit surfaces. New York: Springer.

Raju, M. S. 2005 Numerical investigation of various atomization models in the modeling of a spray flame. *NASA/CR - 2005-214033.*

Sallam, K. A., Aalburg, C. & Faeth, G. M. 2004 Breakup of round nonturbulent liquid jets in gaseous crossflow. *AIAA Journal.* **42** (12), 2529–2540.

Sethian, J. A. 1999 Level set methods and fast marching methods. Cambridge, UK: Cambridge University Press.

Scardovelli, R. & Zaleski, S. 1999 Direct numerical simulation of free-surface and interfacial flow. *Ann. Review Fluid Mechanics* **31**, 567–603.

Sussman, M., Smith, K. M., Hussaini, M. Y., Ohta, M. & Zhi-Wei, R. 2007 A sharp interface method for incompressible two-phase flows. *J. Comp. Phys.* **221**, 469–505.